

Analysing the nanoporous structure of aramid fibres

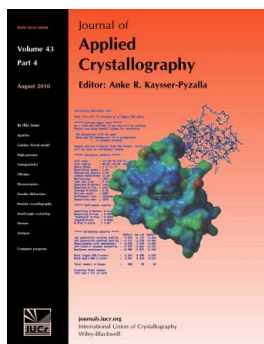
Brian R. Pauw, Martin E. Vigild, Kell Mortensen, Jens W. Andreasen and Enno A. Klop

J. Appl. Cryst. (2010). **43**, 837–849

Copyright © International Union of Crystallography

Author(s) of this paper may load this reprint on their own web site or institutional repository provided that this cover page is retained. Reproduction of this article or its storage in electronic databases other than as specified above is not permitted without prior permission in writing from the IUCr.

For further information see <http://journals.iucr.org/services/authorrights.html>



Many research topics in condensed matter research, materials science and the life sciences make use of crystallographic methods to study crystalline and non-crystalline matter with neutrons, X-rays and electrons. Articles published in the *Journal of Applied Crystallography* focus on these methods and their use in identifying structural and diffusion-controlled phase transformations, structure–property relationships, structural changes of defects, interfaces and surfaces, *etc.* Developments of instrumentation and crystallographic apparatus, theory and interpretation, numerical analysis and other related subjects are also covered. The journal is the primary place where crystallographic computer program information is published.

Crystallography Journals **Online** is available from journals.iucr.org

Analysing the nanoporous structure of aramid fibres

Brian R. Pauw,^{a,b*} Martin E. Vigild,^a Kell Mortensen,^c Jens W. Andreasen^b and Enno A. Klop^d

^aDanish Polymer Centre, Department of Chemical and Biochemical Engineering, Technical University of Denmark, DK-2800 Kongens Lyngby, Denmark, ^bSolar Energy Programme, Risø National Laboratory for Sustainable Energy, Technical University of Denmark, PO 49, DK-4000 Roskilde, Denmark, ^cDepartment of Basic Sciences and the Environment, Faculty of Life Sciences, University of Copenhagen, 1871 Frederiksberg C, Denmark, and ^dTeijin Aramid BV, Fiber Physics Group, 6802 ED Arnhem, The Netherlands. Correspondence e-mail: brian@stack.nl

After consideration of the applicability of classical methods, a novel analysis method for the characterization of fibre void structures is presented, capable of fitting the entire anisotropic two-dimensional scattering pattern to a model of perfectly aligned, polydisperse ellipsoids. It is tested for validity against the computed scattering pattern for a simulated nanostructure, after which it is used to fit the scattering from the void structure of commercially available heat-treated poly(*p*-phenylene terephthalamide) fibre and its as-spun precursor fibre. The application shows a reasonable fit and results in size distributions for both the lengths and the widths of the ellipsoidal voids. Improvements to the analysis methods are compared, consisting of the introduction of an orientation distribution for the nano-ellipsoids, and the addition of large scatterers to account for the effect of fibrillar scattering on the scattering pattern. The fit to the scattering pattern of as-spun aramid fibre is improved by the introduction of the large scatterers, while the fit to the scattering pattern obtained from the heat-treated fibre improves when an orientation distribution is taken into account. It is concluded that, as a result of the heat treatment, the average width and length of the scatterers increase.

© 2010 International Union of Crystallography
Printed in Singapore – all rights reserved

1. Introduction

Aramid fibres are an example of a high-performance polymer material that is used in many applications. The fibres are spun from a liquid crystalline solution of poly(*p*-phenylene terephthalamide) (PPTA) in sulfuric acid (Tanner *et al.*, 1989). In this spinning process, the liquid crystalline solution is forced through a spinning head which contains small spinning holes, each producing its own jet of spinning solution (Weyland, 1980). After traversing a small air gap, the polymer jets enter a coagulation bath in which the polymer undergoes a phase transition due to solvent exchange and changes in temperature. Here, each jet solidifies as a filament, and thus the fibre (a collection of filaments, also known as a yarn) is formed. Structure formation, therefore, mainly occurs in the air gap and coagulation bath (Northolt & Sikkema, 1991). After several washing and drying steps following the coagulation procedure, the fibre (essentially a bundle of filaments) is then ready for immediate use or can be subjected to heat-treatment and stretching steps, which affect the final properties of the material.

The structure of this material can be subdivided into several structural levels. One filament of material is approximately 12 µm in diameter. The filaments *may* exhibit an internal core–shell structure, where the structure in the core of the filament

is significantly different from the structure in the shell of the material (Davies *et al.*, 2008; Panar *et al.*, 1983; Morgan *et al.*, 1983; Horio *et al.*, 1984). Inside this filament we find several levels of fibrillar structure (Morgan *et al.*, 1983; Northolt & Sikkema, 1991; Jiang *et al.*, 1993; Sawyer *et al.*, 1993), with each fibril composed of connected crystallites (Morgan *et al.*, 1983). The crystallites are monoclinic with unit-cell angles of 90°. The crystallite size is approximately 50 × 50 × 200 Å (Northolt & Sikkema, 1991; Northolt & van Aartsen, 1973; Jackson *et al.*, 1994) and the crystal density is 1.48 g cm⁻³ (Northolt & Stuut, 1978; Yabuki *et al.*, 1976). The material in the fibres is highly crystalline, as no amorphous halo is observed in the diffraction pattern (Northolt & Sikkema, 1991; Panar *et al.*, 1983). Furthermore, the crystallites are radially aligned in the sample to a certain extent, with the crystallographic *b* axes pointing towards the centre of the material (Riekell *et al.*, 1997).

In addition to this structure there is considerable evidence for the presence of a nanoporous structure in the filaments (Mooney & MacElroy, 2004; Northolt & Sikkema, 1991; Jiang *et al.*, 1993; Aerts, 1991; Saijo *et al.*, 1994). Firstly, there is the difference between the crystalline density of PPTA (1.48 g cm⁻³) and the macroscopic density of the material (which ranges from 1.45 to 1.47, depending on the production process) (Jiang *et al.*, 1993; Northolt & Sikkema, 1991; Chae & Kumar, 2006). The absence of an amorphous diffraction signal

indicates that little or no amorphous PPTA is present, so that the reduced density is likely to be due to about 5 vol.% of voids. Secondly, direct observations of a porous structure have been obtained through transmission electron microscopy by (amongst others) Dobb *et al.* (1979). In other investigations the moisture uptake in the filaments is analysed. The moisture is partially transported through and stored in a void structure (Saijo *et al.*, 1994; Mooney & MacElroy, 2004). Finally, the presence of a strong small-angle X-ray scattering (SAXS) signal strongly supports the presence of voids, especially since it is dependent on the moisture content (Dobb *et al.*, 1979; Saijo *et al.*, 1994). The void structure appears analogous to that found in carbon fibres (Dobb *et al.*, 1977), although it exhibits a lower aspect ratio (Northolt & Sikkema, 1991). An alternative explanation for the existence of the SAXS signal is that this signal could also originate from an amorphous phase instead of a void structure (Ran *et al.*, 2001; Grubb *et al.*, 1991). Ran *et al.* (2001) reached this conclusion partially since they did not observe a change in the SAXS pattern when subjecting PPTA fibres to moisture. In view of the investigations referred to above, it is at present commonly accepted that a void system is present in the fibres.

The characteristics of the nanostructure are strongly correlated with the physical properties of the material (Kenig, 1987; Picken *et al.*, 1992; Rao *et al.*, 2001a). Investigations using crystallography and tensile testing have shown that the orientation of the yarn is directly related to the dynamic compliance (inverse of the sonic modulus) (Northolt & Sikkema, 1991). In the same (review) article, it is also argued that the strength of the aramid fibre is governed by the effect of inhomogeneities and impurities. Most clearly, many properties of the fibre are affected by heat-treatment procedures (Jackson *et al.*, 1994; Rao *et al.*, 2001b).

SAXS is an ideal tool for the study of the nanoporous structure in these fibres. Practically, however, the analysis of the scattering data is rather complex. Complicating factors for this type of sample are the polydispersity in size, shape and orientation of the scatterers, resulting in a smoothly decaying, anisotropic scattering pattern (Dobb *et al.*, 1979). Previous analysis methods have focused on limiting the analysis to regions of the scattering patterns to obtain physically relevant parameters (Perret & Ruland, 1970; Grubb *et al.*, 1991).

Whilst many data are left unused when analysing only a small segment of the data, few analysis techniques exist that are capable of analysing the full two-dimensional scattering pattern to use the remaining data without bias. Of note is the two-dimensional analysis method by Helfer *et al.* (2005), who simulated the scattering pattern from imperfectly aligned monodisperse cylindrical scatterers with finite length, oriented according to a Maier–Saupe orientation distribution. Additionally, Stribeck (2001) uses two-dimensional chord distribution functions (a form of the interface distribution function, adapted to study highly anisotropic materials) to visualize the structural parameters extracted from the scattering patterns in real space.

This paper focuses on the methodology development for the analysis of the full two-dimensional scattering patterns

obtained from aramid fibres. Its merit is tested in relation to the already available methods, as well as to simulations. Lastly, its applicability is shown when applied to a commercial aramid fibre and its precursor.

2. Experimental

2.1. Sample preparation

Two samples are considered, one so-called ‘as-spun’ material that has not undergone a tensioned heat-treatment procedure, and the commercially available aramid fibre Twaron 1000. The as-spun material can be viewed as a precursor to the commercially available fibre. Both samples consist of a bundle of PPTA filaments and were obtained from Teijin Aramid BV. The samples did not contain spin finish. The samples are mounted on rectangular frames of 13 × 18 mm in size, similar to the method described by Hermans *et al.* (1959). The frames hold an average of about 1000 filaments per mm.

All samples were prepared at least one week before the synchrotron SAXS measurements, and they were dried in vacuum before transportation in a box kept dry with silica gel. Upon arrival at the synchrotron facility, the samples were stored in vacuum to prevent the uptake of moisture.

2.2. Beamline details

Synchrotron experiments were performed at the I711 beamline at the MAX-lab synchrotron in Lund, Sweden. The collimation was a square collimation, 0.5 × 0.5 mm in size. The wavelength used was 1.235 Å, with a sample-to-detector distance of 1.449 m. The scattering patterns were recorded using a Marresearch 165 CCD detector, quantized into 2048² pixels. Transmission values (where applicable) were determined using a beamstop-mounted detector.

2.3. Determination of coefficient of variance using a laboratory source

In order to determine the coefficient of variance for some model fits, five frames of Twaron 1000 and five frames of as-spun Twaron were measured for 1 h on the Risø DTU SAXS instrument. This instrument consists of a rotating-anode generator running with a copper anode producing radiation with a wavelength of 1.5418 Å (Cu K α). The beam is collimated to a diameter of 1 mm using pinholes. The sample-to-detector distance was set to 1.45 m. The detector is a Gabriel-type wire detector, quantized into 1024² pixels. Transmission values were determined by detecting fluorescence orthogonal to the beam of an iron foil which can be placed in front of the beamstop. The coefficients of variance were calculated by comparing the fitting parameters obtained from analysis of the measured data from each frame. The coefficient of variance (CV) is defined as the standard deviation normalized to the mean.

3. Classical analyses

The literature provides several analysis methods that can be applied for determining the orientation of scatterers in the

sample and for the determination of the average size parameters of the scatterers. We will refer to two methods that have classically been used to determine the orientation parameters. These two methods are the invariant-based method and the ‘Ruland streak’ method. For the determination of size parameters several options are available, namely the Guinier, Debye–Bueche and Porod methods.

3.1. Orientation analysis through the Effler invariant method

An invariant-based orientation parameter determination for samples with fibre symmetry has been developed by Effler & Fellers (1992). They noted that the invariant for anisotropic scattering patterns has a different meaning than for isotropic samples. For anisotropic samples, the (direction-dependent) invariant Q_ψ , defined as

$$Q_\psi = \int_0^\infty q^2 I(q, \psi) dq, \quad (1)$$

is a measure of the square of the average electron-density distribution in the direction ψ , where q is the momentum transfer, defined as $q = (4\pi/\lambda) \sin \theta$ with λ the wavelength of the incident radiation and 2θ the scattering angle. In the numerical implementation of the integration in this report, no extrapolation to $q = 0$ and $q = \infty$ is performed for this determination. Analysis of the variation of Q_ψ as a function of ψ using equation (1) results in the expression of the orientation parameter as $\langle \sin^2 \psi \rangle$ or the Hermans orientation parameter F_H through $F_H = 2\langle \sin^2 \psi \rangle - 1$:

$$\langle \sin^2 \psi \rangle = \frac{F_H + 1}{2} = \frac{\int_0^{\pi/2} Q_\psi \sin^2 \psi d\psi}{\int_0^{\pi/2} Q_\psi d\psi}. \quad (2)$$

This equation can be numerically evaluated using a sufficiently small step size. For a perfectly oriented scatterer, $\langle \sin^2 \psi \rangle$ is 1, and for randomly oriented scatterers this is 0.5 (corresponding to an F_H of 1 and 0, respectively).

3.2. Orientation analysis through the Ruland streak method

The degree of alignment of scatterers can also be obtained using the so-called Ruland streak method. This method was proposed by Perret & Ruland (1969). Wang *et al.* (1993) have applied the method to as-spun PPTA fibres that have been subjected to critical-point carbon dioxide drying. The method assumes well oriented scatterers with a high aspect ratio, for example needle-like voids as found in carbon fibres. The main scattering contribution is found along the normal of the main axis of the scatterer. A single scatterer will produce a scattering streak along this normal. A rotation of the main axis of the scatterer in the plane of the detector will see a similar rotation of the streak. Thus, the distribution G_N of the normals of the scatterers in the detector plane can be directly measured.

The method consists of determining the integral breadths of azimuthal regions (*i.e.* domains at constant q). The integral breadths are defined as

$$B_{\text{obs}}(q) = \frac{\int_{\psi_{\text{max}} - \pi/2}^{\psi_{\text{max}} + \pi/2} I(q, \psi) d\psi}{I(q, \psi_{\text{max}})}. \quad (3)$$

The error of this computation is defined as

$$\varepsilon_b = \left[\sum_\psi I(q, \psi) \right]^{1/2} + [I(q, \psi_{\text{max}})]^{1/2} \quad (4)$$

where B_{obs} is the observed integral breadth of the azimuthal profile, ψ_{max} is the angle at which the peak maximum is found and $I(q, \psi)$ is the background-corrected intensity. Thus, the integral breadth provides a means of quantifying the width of the azimuthal profile, irrespective of the peak shape. It remains sensitive to noise, however, which for regions of low intensity can increase the integral breadth.

It was noted by Perret & Ruland (1969) that this observed integral breadth is equal to the breadth of the distribution of the normals of the scatterers and should thus be independent of q . This is true for infinitely long scatterers. For scatterers with finite length, there is an additional contribution, present mainly at low q , originating from the length L of the scatterers. This contribution is dependent on q . For a Gaussian orientation distribution of the axes of the scatterers, the observed integral breadth B_{obs} is related to q , L and the integral breadth of the normals of the scatterers B_ψ by

$$B_{\text{obs}}^2 = B_\psi^2 + \frac{4\pi^2}{L^2 q^2}. \quad (5)$$

This holds for relatively narrow orientation distributions. For a Lorentzian (Cauchy-like) orientation distribution of the axes, this becomes

$$B_{\text{obs}} = B_\psi + \frac{2\pi}{Lq}. \quad (6)$$

Both equations are applied when analysing the experimental data and are fitted to the B_{obs} versus q data. The equation that describes best the observed values of B_{obs} is the most likely candidate in terms of type of orientation distribution (Striebeck, 2007).

3.3. The Debye–Bueche correlation length determination

It has been established that approximating methods developed for isotropic systems are also applicable to systems with fibre symmetry (Ruland, 1978). This implies that, for example, the Debye–Bueche method for random interfaces (Debye & Bueche, 1949; Debye *et al.*, 1957) can be applied to oriented systems. The method is then to be applied to the unprojected data in a certain direction (*e.g.* perpendicular to the fibre axis), and the results are then only valid for the nanostructure in that particular direction (Ruland, 1978). The Debye–Bueche scattering function for a system of random interfaces is expressed as (Debye & Bueche, 1949)

$$I(q) = \frac{I_0}{(1 + q^2 L_c^2)^2} + I_{\text{fl}} \quad (7)$$

where I_0 is an intensity scaling factor, L_c is the Debye correlation length (a characteristic size parameter related to the

mean lengths between interfaces present in the sample) and I_{fl} is a constant, modelling the scattered intensity from electron-density fluctuations in the phases according to Ruland (1971).

If there are two distinct, non-interacting distributions of interfaces originating from objects of considerably different sizes (*i.e.* if the sample contains scatterers with a bimodal size distribution), then the two can be considered to have separate, independent contributions to the scattering intensity. With relevance to our study, these two objects of considerably different sizes could consist of (1) a structure of fibrils with interfibrillar voids and (2) a nanoporous structure of (much smaller) voids inside the fibrils. Under this assumption, a ‘double Debye’ function can be construed:

$$I(q) = \frac{I_{0a}}{(1 + q^2 L_{c1}^2)^2} + \frac{I_{0b}}{(1 + q^2 L_{c2}^2)^2} + I_{fl}. \quad (8)$$

3.4. The Porod length determination

The Porod relationship applicable for scattering from smooth interfaces is expressed as

$$I(q) = \frac{K_p}{q^4} + I_{fl} \quad (9)$$

for sufficiently large q and K_p is the Porod constant, a scaling factor proportional to the surface-to-volume ratio and the scattering contrast. Here too, the fluctuation term I_{fl} has been added (Ruland, 1971).

A size parameter L_p can be determined from a Porod fit applied to data on an arbitrary intensity scale, through

$$L_p = \frac{\pi \int_0^\infty I(q) q \, dq}{Q}. \quad (10)$$

To evaluate this equation, the first moment (numerator) and the invariant (denominator) have to be determined. The invariant is defined as (Glatter & Kratky, 1982)

$$Q = \int_0^\infty q^2 I(q) \, dq \quad (11)$$

and can be obtained through evaluating the invariant for the intensity described by both the Debye function [equation (7),

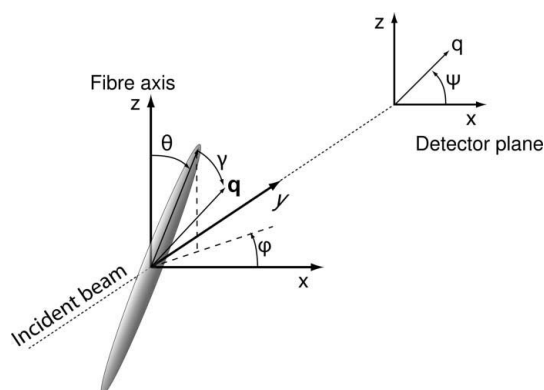


Figure 1
Diffraction geometry used in the model description.

without fluctuation terms as indicated by Ruland (1990)], and the Porod function [equation (9)], bounded by the crossover limit q_{co} :

$$\int_0^{q_{co}} \frac{I_0 q^2}{(1 + q^2 L_c^2)^2} \, dq = \frac{I_0}{2L_c^2} \left[\arctan(L_c q_{co}) - \frac{L_c q_{co}}{L_c^2 q_{co}^2 + 1} \right] \quad (12)$$

and

$$\int_{q_{co}}^\infty \frac{q^2 K_p}{q^4} \, dq = \frac{K_p}{q_{co}}. \quad (13)$$

The total invariant Q then is

$$Q = \frac{I_0}{2L_c^2} \left[\arctan(L_c q_{co}) - \frac{L_c q_{co}}{L_c^2 q_{co}^2 + 1} \right] + \frac{K_p}{q_{co}}. \quad (14)$$

The numerator of equation (10) is derived in a similar manner as Q :

$$\pi \int_0^\infty I(q) q \, dq = \pi \left[-\frac{1}{2(q_{co}^2 L_c^3 + L_c)} + \frac{1}{2L_c} + \frac{K_p}{2q_{co}^2} \right]. \quad (15)$$

3.5. Model setup

3.5.1. Model basis. A new analysis model is built up around a system of well oriented ellipsoidal scatterers, independently polydisperse in both the long and short axes of the (rotational) ellipsoids. This is a modification of the method of Helfer *et al.* (2005), who modelled a system of oriented, monodisperse, cylindrically shaped scatterers. The full description for the scattering intensity of a system of polydisperse oriented scatterers is

$$I(\mathbf{q}) = I(q, \psi) = C_1 \int_0^\infty \int_0^\infty V(R_1, R_2)^2 \int_0^{2\pi} \int_0^{\pi/2} F^2(q, R_1, R_2, \gamma) \times h(\theta) \sin \theta \, d\theta \, d\varphi \, f(R_1) g(R_2) \, dR_1 \, dR_2 \quad (16)$$

where \mathbf{q} is the scattering vector. In the tangent plane approximation its magnitude is q and ψ is the angle on the detector (Fig. 1). θ is the angle between the fibre axis and the long axis of the ellipsoid, and φ is the angle between the projection of the long axis on the xy plane and the x axis. F is the form factor of the scatterer and C_1 is a scaling factor. The diffraction geometry is graphically displayed in Fig. 1. γ is the angle between \mathbf{q} and the main ellipsoid axis. The angles are related through (Helfer *et al.*, 2005)

$$\cos \gamma = \cos \theta \sin \psi + \sin \theta \cos \psi \cos \varphi. \quad (17)$$

The distribution $h(\theta)$ is the orientation distribution of the scatterers with respect to the fibre axis, and $f(R_1)$ and $g(R_2)$ are the radius distributions for the ellipsoidal scatterers, one describing the short-axis radius (R_1), and the other describing the long-axis radius of the ellipsoid (R_2). The size distributions $f(R_1)$ and $g(R_2)$ are expressed using the log-normal probability density function $P(R)$, commonly used to describe particle size

distributions and defined as (Weisstein, 2005; Crow & Shimizu, 1988)

$$P(R) = \frac{1}{RS(2\pi)^{1/2}} \exp\left\{-\frac{[\ln(R) - M]^2}{2S^2}\right\}. \quad (18)$$

The parameters S and M are related to the mean μ and variance σ of the distribution through

$$M = \ln\left[\frac{\mu^2}{(\sigma + \mu^2)^{1/2}}\right], \quad (19)$$

$$S = \left[\ln\left(\frac{\sigma}{\mu^2} + 1\right)\right]^{1/2}.$$

For numerical purposes, it is more convenient to use the orientation distribution function $\tilde{h}(\theta)$, defined as

$$\tilde{h}(\theta) = 2\pi \sin\theta h(\theta). \quad (20)$$

In this report, we initially assume a perfect orientation of the scatterers, and therefore the description of the two-dimensional scattering intensity simplifies to

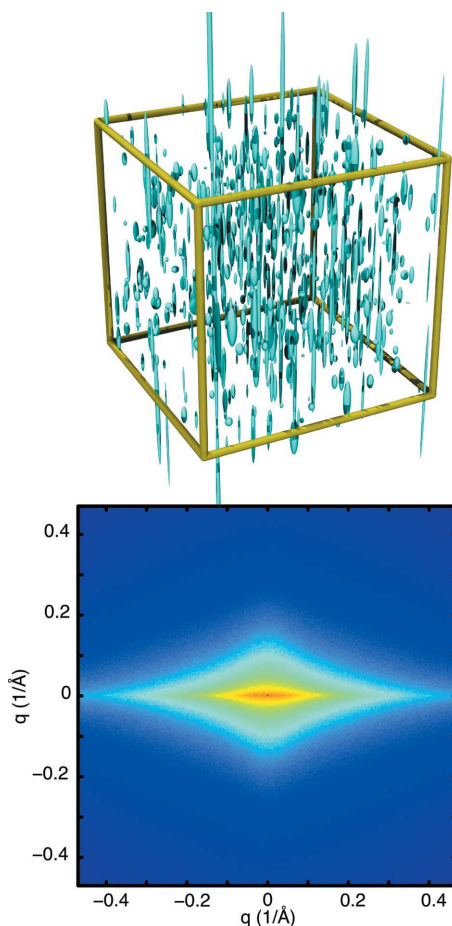


Figure 2

An example of a simulated pore system consisting of a volume filled with perfectly oriented ellipsoids (top), and the resulting scattering pattern computed from 100 such simulations (bottom, main ellipsoid axes vertical). The size parameters used in the simulation are $f(R_1) \mu = 17.7$, $f(R_1) \sigma = 50.4$, $g(R_2) \mu = 96.6$, $g(R_2) \sigma = 7560$ and a volume fraction of 0.1%. Intensity shown on a logarithmic scale.

$$I(q, \psi) = C_2 \int_0^\infty \int_0^\infty V(R_1, R_2)^2 \times F^2(q, \psi, R_1, R_2) f(R_1) g(R_2) dR_1 dR_2 \quad (21)$$

where C_2 is a scaling factor. Note that γ in the form factor has been replaced with ψ , as equation (17) simplifies to $\cos\gamma = \sin\psi$ when perfectly aligned ellipsoids are assumed (*i.e.* $\theta = 0$).

The form factor of a rotational ellipsoidal scatterer is obtained as a modification of the form factor of a sphere. This can be achieved by replacing the sphere radius R in the Rayleigh scattering function by R_{ell} , defined as (Pedersen, 1997; Guinier & Fournet, 1955)

$$R_{\text{ell}} = (R_1^2 \sin^2 \gamma + 4R_2^2 \cos^2 \gamma)^{1/2}. \quad (22)$$

We then obtain for the form factor of our ellipsoidal scatterer

$$F(q, \psi, R_1, R_2) = 3 \frac{\sin(qR_{\text{ell}}) - qR_{\text{ell}} \cos(qR_{\text{ell}})}{(qR_{\text{ell}})^3}. \quad (23)$$

Note that a structure factor is not included in the scattering function [equation (21)]. This has been done since the ellipsoidal void structure is assumed to be non-interacting and the individual scatterers are able to intersect. One could expect some typical distance between voids imposed by for example crystal sizes or fibrillar sizes, but the observed small-angle scattering gives no indication of such characteristics. This implies that no volume is excluded, and no structure is imposed at higher scatterer concentrations. A structure factor is therefore not considered.

The fitting procedure is carried out using a prototype open-source SAXS analysis package named *SAXSGUI*, developed by Dr Joensen of JJ X-ray Systems A/S in collaboration with Rigaku and several individual contributors. The data are linearly binned using bins containing 4×4 image pixels. The q -range fit is 0.025 – 0.25 \AA^{-1} , and the ψ range extends 90° to either side of the main axis of the scattered streak. The minimization function is a least-squares residual function:

$$\chi^2 = \frac{\sum_{i=1}^N (I_{\text{model}} - I_{\text{measurement}})^2}{N - n_{\text{param}}} \quad (24)$$

where i is the datapoint index, N is the total number of data points in the fit and n_{param} is the number of fitting parameters.

The intensity I_{model} for each q and ψ value in the data is interpolated (using a two-dimensional linear interpolation routine) from the intensity of an equidistant q, ψ grid spanning 180° in ψ , which spans the q range of the data to be fitted. The number of grid points in the ψ direction is set to 180 and the number of grid points in q can be adjusted by the user. Using 20 grid points in q is found to provide a sufficiently fine grid.

3.5.2. Simulation setup. In order to verify the applicability of some of the analysis methods, scattering patterns have been numerically simulated. To achieve this, a three-dimensional box is filled with perfectly aligned non-interacting rotational ellipsoids, polydisperse in both the short radius and the long radius using separate log-normal distributions (see Fig. 2, top).

The positioning of the ellipsoids within the box is purely random. In order to suppress edge effects (from truncated ellipsoids) during the Fourier transform procedure, the ellipsoids that cross the box boundaries are subject to periodic boundary conditions. The box is divided into 300^3 voxels, Fourier transformed, and convoluted with a sinc function (Fourier transform of a voxel) similar to the method described by Schmidt-Rohr (2007).

The first row of parameters listed in Table 1 is used for initial tests. The other listed values offer values for aspect ratio tests that are used to determine the effects of aspect ratio on the orientation distribution analysis methods. Each simulated scattering pattern consists of the average of 100 invocations of the simulation (*i.e.* the structure is regenerated and its scattering pattern computed 100 times).

The obtained simulated scattering patterns (such as shown in Fig. 2, bottom) can now be used to test the applicability of some of the models. The scattering pattern in the example shown in Fig. 2 shows cuspidal features, not commonly associated with scattering from oriented ellipsoids (Ciccariello *et al.*, 2002). This behaviour is due to the consideration of polydispersity in both the short axis and the long axis of the ellipsoids, resulting in contributions from ellipsoids with a range of aspect ratios.

3.5.3. Model adaptations. Adaptations to the model which will be discussed below include an implementation of an orientation distribution of the ellipsoids and the addition of large-sized scatterers to the log-normal distributions to approximate a bimodal distribution.

The orientation distribution has been implemented as a rotational smearing of the modelled scattering pattern [equation (21)] in ψ . This amounts to a rotation of the ellipsoids only in the xz plane (*i.e.* assuming $\varphi = 0$). This has been done to speed up the calculation of the rotationally smeared intensity (as an additional numerical integration over φ would significantly increase the computational time), and yields results that approximate the orientation distribution of the normals of the ellipsoidal scatterers. This approximation is valid *only* for small widths of the orientation distribution.

The rotational smearing is achieved in the calculation of I_{model} by applying a circular matrix shift to the q, ψ matrix in the ψ direction. Owing to the number of grid points in ψ , a shift by $n = 1$ corresponds to a 1° rotation. Summing the thus shifted intensity after multiplying with the orientation distribution P results in intensity that is rotationally smeared in ψ :

$$I_{\text{OD}}(q, \psi) = \sum_{n=0}^{180} I_n(q, \psi)P(n). \quad (25)$$

Here, $I_n(q, \psi)$ is the q, ψ grid after a circular matrix shift of n° . $I_{\text{OD}}(q, \psi)$ is the scattering pattern with the orientation distribution implemented.

The orientation distribution $P(\zeta)$ is the distribution of the normals to the scatterers, where ζ is the angle between the normal and the direction $\psi = 0$. It is implemented here as a von Mises distribution function (Weisstein, 2009; Evans *et al.*, 2000), modified for high values of κ by P. Malchev at Teijin

Table 1
Simulation parameters.

$f(R_1) \mu$	$f(R_1) \sigma$	$g(R_2) \mu$	$g(R_2) \sigma$	Volume fraction	Approximate aspect ratio
17.7	50.4	96.6	7560	0.01	5.45
20	50	2	5	5×10^{-4}	0.1
20	50	4	10	1×10^{-3}	0.2
20	50	10	25	2.5×10^{-3}	0.5
20	50	20	50	5×10^{-3}	1
20	50	40	100	0.01	2
20	50	100	250	0.025	5
20	50	200	500	0.05	10
20	50	2000	5000	0.1	100

Aramid. For the probability density distribution function in degrees, we use

$$P(\zeta) = \begin{cases} \frac{\kappa \exp[\kappa \cos(\zeta 2\pi/360)]}{2\pi \cdot 2\pi J(0, \kappa)} & \text{if } \kappa \leq 100 \\ \frac{\kappa}{2\pi} \exp[\kappa \cos(\zeta 2\pi/360)] & \text{if } \kappa > 100 \end{cases} \quad (26)$$

where J is the Bessel function of the first kind and κ is an inverse measure of the width of the orientation distribution. Fig. 3 shows an example of the scattering pattern calculated for a system of highly elongated particles with an orientation distribution having a κ value of 100.

The second adaptation is the addition of large scatterers. For some materials that will be described below, a significant amount of scattering at low q reduces the fitting capability of the model. This extra scattering at low q is taken into account by the addition of a large, slightly polydisperse (to reduce oscillatory behaviour) ellipsoid to the model. Such large scatterers could be related to a more pronounced fibrillar structure present in these fibres. This is implemented by adding to the intensity obtained from the model [equation (21)] a contribution for large scatterers with a distribution for the short-axis radius R_{L1} and long-axis radius R_{L2} , *i.e.*

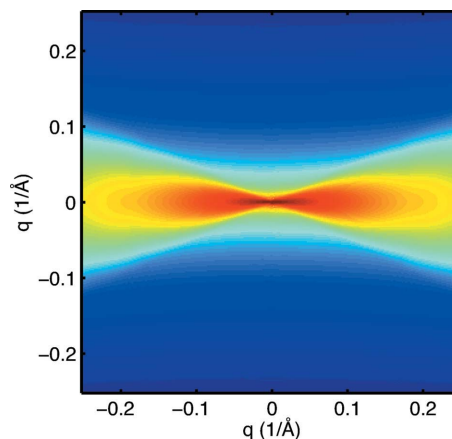


Figure 3
The effect of an orientation distribution on the scattered intensity from elongated ellipsoids, as computed with the fitting model with ellipsoid distribution parameters $f(R_1) \mu = 25$, $f(R_1) \sigma = 50$, $g(R_2) \mu = 1000$, $g(R_2) \sigma = 1000$ and a von Mises κ of 100 (which has an FWHM of 13.6°). Intensity shown on a logarithmic scale.

$$I_{\text{adapted}}(\mathbf{q}) = I[\mathbf{q}, f(R_1), g(R_2)] + C_3 I[\mathbf{q}, f(R_{L1}), g(R_{L2})] \quad (27)$$

where C_3 is the scaling factor for the intensity from the large scatterers. The distribution for the large scatterers is linked to the aspect ratio α through

$$g(R_{L2}) = \alpha f(R_{L1}) \quad (28)$$

and the width of the distribution is fixed to small values (sufficiently large to dampen oscillatory behaviour), so that only the short-axis radius R_{L1} , aspect ratio α and scaling factor C_3 are added as fitting parameters.

The third adaptation combines both previous adaptations into a single model.

4. Results and discussion

4.1. Classical and new data analysis models applied to a measurement of Twaron 1000

4.1.1. Twaron 1000 measurement. The applicability of the methods was tested on a 30 min measurement of Twaron 1000 (the two-dimensional scattering pattern of this sample is shown in logarithmic and linear intensity scale in Fig. 11).

4.1.2. Effler invariant method. Analysis of the measured scattering pattern using the Effler invariant method in the q range 0.03–0.2 \AA^{-1} results in an orientation parameter value of $\langle \sin^2 \psi \rangle = 0.899$ (3). This value is the average over all four quadrants. The corresponding Hermans orientation factor F_H is 0.80.

An analysis of the simulated data shown in Fig. 2 of polydisperse, perfectly aligned ellipsoids with a relatively low aspect ratio results in an orientation parameter value of $\langle \sin^2 \psi \rangle = 0.881$ (9). This result for a perfectly aligned system shows that the Effler invariant method is sensitive to the aspect ratio of the scatterers, which affects the intensity in the directions off-normal to the scatterers. This effect may be investigated more closely, *i.e.* by plotting the $\langle \sin^2 \psi \rangle$ value as a function of mean aspect ratio for several simulations of perfectly oriented, polydisperse ellipsoidal scatterers, resulting in the diagram as shown in Fig. 4. The point at an

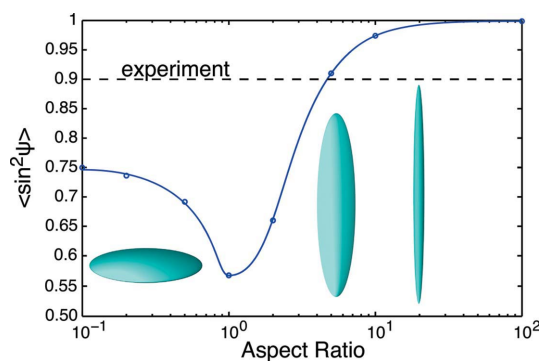


Figure 4 $\langle \sin^2 \psi \rangle$ determined *via* the Effler invariant method with parameters given in Table 1, *versus* the mean aspect ratio for scattering patterns obtained from simulations of perfectly oriented, polydisperse ellipsoidal scatterers. The dashed line indicates the experimentally found value for Twaron 1000, the solid line is a Bezier curve drawn to guide the eye.

aspect ratio of 1 indicates a value of $\langle \sin^2 \psi \rangle = 0.56$. Note that separate size distributions were used for the length and the width, and that therefore the aspect ratio in Fig. 4 is the average of all scatterers.

From this figure, and given the experimental value of $\langle \sin^2 \psi \rangle = 0.899$, we find that the mean aspect ratio of the scatterers in the sample must lie above ~ 5 . If the sample were to contain scatterers with much larger aspect ratios, the introduction of an orientation distribution of these scatterers will lower the $\langle \sin^2 \psi \rangle$ value to reach the found value of 0.899.

Thus, through the analysis presented above, it has been established that the sample contains well oriented scatterers, with a mean aspect ratio larger than 5.

4.1.3. Ruland streak method. For the application of the Ruland streak method, the q space ($q = 0.01$ – 0.25\AA^{-1}) has been divided into 40 azimuthal sections (*i.e.* with a width of $\Delta q = 0.006 \text{\AA}^{-1}$). For each section, the integral breadth has been determined using all data points within that section. The result is shown as the blue dotted line in Fig. 5.

The streak methods, based on both Gaussian and Lorentzian distributions, fit poorly to the data. The best fitting profile is that of a Lorentzian distribution of the scatterer normals. The integral breadth B_ψ that is obtained is a value that approaches the integral breadth of the azimuthal curve of the 200 reflection of the PPTA crystallites (found to be 14.8° for Twaron 1000). The length that is determined through the streak method (5.9 or 8.0\AA) appears unrealistically small, as will become apparent in the next paragraphs. Since the fit is also relatively poor, it cannot be considered to be accurate.

Wang *et al.* (1993) have shown a successful application of the streak method applied to critical-point-dried (CPD) as-spun aramid fibre. However, our results indicate that the streak method is not exceptionally suited for the analysis of the nanostructure of the aramid fibres studied here, which is also supported by the absence of the ‘butterfly-like’ intensity map often encountered in SAXS data subjected to this analysis. The reason for the poor applicability is that the broadening at low angles can no longer be solely ascribed to the length of the scatterer, but also has contributions from the

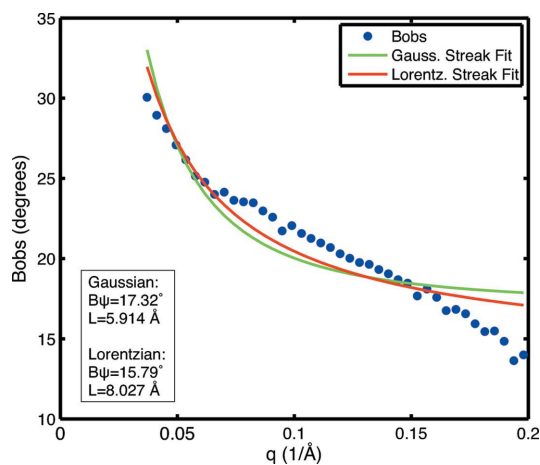


Figure 5 Streak fits to the scattering pattern obtained (at MAX-lab) from a bundle of Twaron 1000 filaments.

sides of the ellipsoids. Additionally, a contribution to the intensity from a separate system of scatterers with a separate orientation distribution (such as highly oriented fibrillar scattering) may affect this determination.

4.1.4. Debye–Bueche analysis. The results of the Debye–Bueche analysis show that the Debye–Bueche model fits reasonably well to the data (shown in Fig. 6) for Twaron 1000. Above $q = 0.09 \text{ \AA}^{-1}$, however, the model fails to describe the data. For the as-spun material, the Debye fit is less satisfactory (*cf.* Fig. 7).

Upon closer investigation of the intensity curve of the as-spun sample (Fig. 7) two slopes can be distinguished in the Debye plot, indicating that we may have interface distributions centred around two distinct sizes. This is where the previously mentioned ‘double Debye’ relationship comes into play. By adding intensity from a second interface distribution function, some of the sizes present may be determined. The result of this is depicted in Fig. 8. The difference in appearance of the intensity in the ‘Debye’ plots is due to a difference in I_{fl} , which has converged to a (too) large value in the fit with the single Debye function (I_{fl} is determined separately when fitting the Debye and Porod functions). We now obtain two correlation lengths, one very large (and most likely unreliable owing to the lack of sufficient data at very low q) and one ordinary size correlation length.

Application of the Debye–Bueche fitting model to the simulated data (shown in Fig. 2) results in a fit similar to that of Twaron 1000, resulting in a correlation length L_c of 11.9 Å. This correlation length is related to the void size L_v through $L_v = L_c(1 - \nu)^{-1}$, where ν is the volume fraction of voids, and therefore the correlation length approaches the void size for low volume fractions. This is very close to the mode (also known as the maximum likelihood estimator) of the radius distribution that was simulated (these distributions are identical to those shown at the end of §4.3; the mode of the short-axis radius is about $R \simeq 14 \text{ \AA}$). When we analyse the intensity scattered in the meridional direction (*i.e.* along the fibre axis), a correlation length of 30.8 Å is obtained. This, again,

approaches the mode of the distribution of the long-axis radius of the scatterer, which is at $R \simeq 40$.

These results show evidence of the applicability of the Debye–Bueche method, returning a value somewhat below the mode of the size distribution. Furthermore, the results for the as-spun material indicate that a standard unimodal correlation function fit is severely affected by large-sized scatterers. The application of a model based on a ‘double Debye’-type bimodal correlation function reveals a significant contribution from large scatterers.

4.1.5. Porod analysis. The Porod analysis for Twaron 1000 is shown in Fig. 6. The fit is less than reliable, as is apparent from the Porod plot (the data should have a linear region at high q). One possible explanation is that the Porod region has not yet been reached in these measurements. Alternatively, there may be a change in the slope, due to graded interfaces (Koberstein *et al.*, 1980), surface roughness (Tang *et al.*, 1986), beginning wide-angle diffraction peaks (Stribeck, 2007) or other Porod

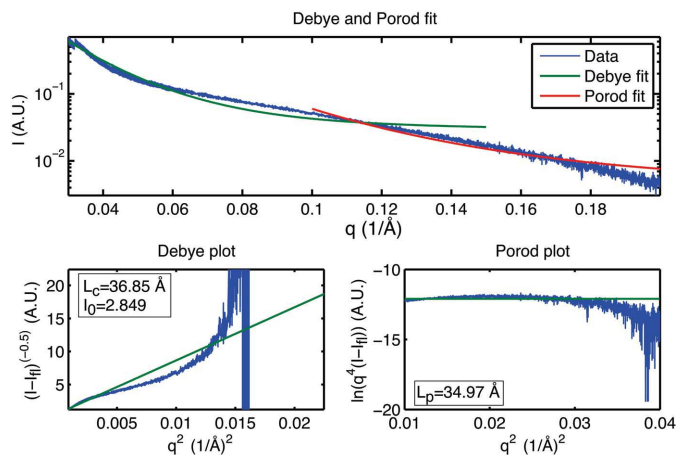


Figure 7 Results from the Debye–Bueche and Porod analysis, as well as the associated Debye and Porod plots applied to the equatorial intensity of as-spun Twaron (a pie section with a width in ψ of 1°).

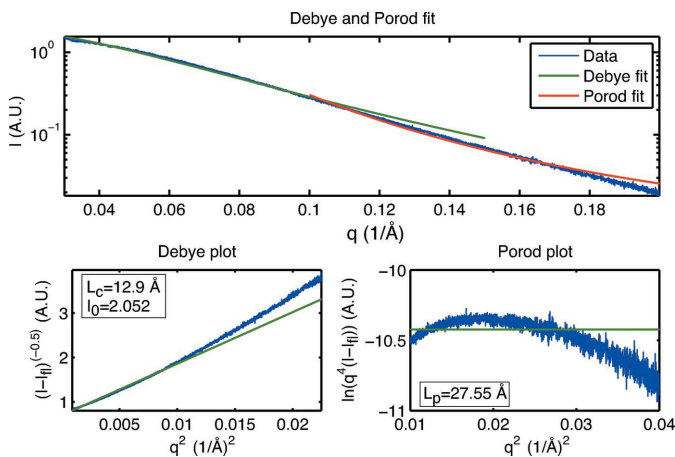


Figure 6 Results from the Debye–Bueche and Porod analysis, as well as the associated Debye and Porod plots applied to the equatorial intensity of Twaron 1000 (a pie section with a width in ψ of 1°).

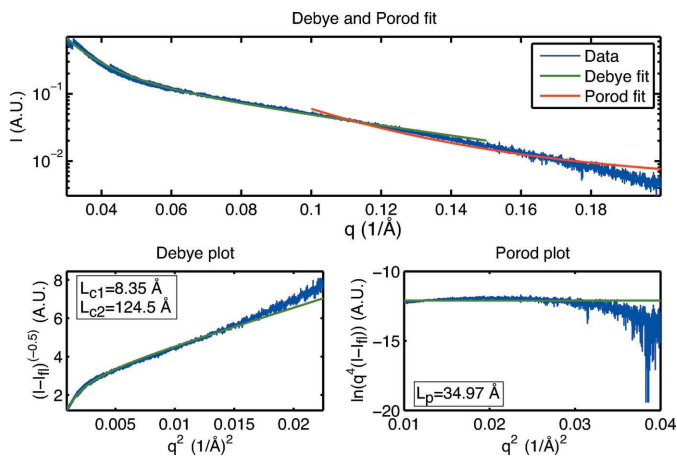
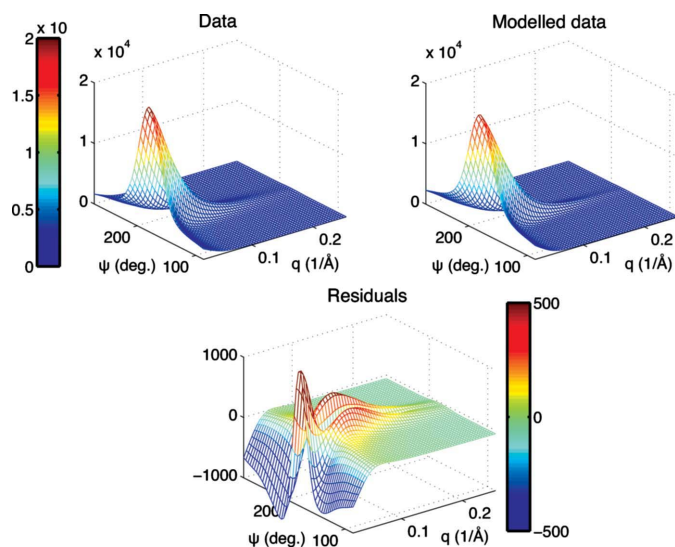


Figure 8 Results from the bimodal Debye–Bueche analysis, as well as the associated Debye and Porod plots applied to the equatorial intensity of as-spun Twaron (a pie section with a width in ψ of 1°).


Figure 9

Intensity plot of the Twaron 1000 measurement, compared with the intensity based on the polydisperse ellipsoid model, leaving a small amount of residual intensity. Residuals are shown on a vertical scale 20 times that of the data.

slope modifications (Diez & Sobry, 1993; Ciccariello, 1993; Ruland, 1971).

The Porod method appears to work a little better for the as-spun material, where before the intensity drop at $q^2 = 0.03 \text{ \AA}^{-2}$ the data are described rather well by the model (*cf.* Fig. 7). The value of the Porod length ($L_p = 28 \text{ \AA}$) resulting from the Twaron 1000 fit does not compare well with the correlation length obtained from the Debye function ($L_c = 13 \text{ \AA}$), whereas for as-spun Twaron this Porod length (of $L_p = 35 \text{ \AA}$) does approach the Debye correlation length (of $L_c = 37 \text{ \AA}$). Since the Porod length value is heavily dependent on the extrapolation of the intensity to $q = 0$ and $q = \infty$, the extrapolation method may be equally at fault. Values for the surface-to-volume ratio have not been determined, as they assume isotropic scatterer orientation.

4.2. Applicability of classical analyses

The results so far indicate that the applicability of the Ruland streak method and the Porod method for the analysis of SAXS data of the investigated aramid yarns is limited. Other classical methods, *i.e.* the Debye–Bueche method and

the Effler invariant method, appear to work well, although for the latter method the aspect ratio of the scatterers must be sufficiently large. In §4.3, the results of our new data analysis method will be presented, which makes use of the full two-dimensional scattering pattern. This method not only allows the extraction of average size parameters from the scattering pattern, but also allows the determination of the complete size distributions of the scatterers in both lateral and longitudinal directions.

4.3. Full two-dimensional data analysis model

Fitting the new model to the Twaron 1000 measurement works very well when done within a q range of $0.025\text{--}0.25 \text{ \AA}^{-1}$ (*cf.* Fig. 9). The parameters included in the fit are C_2 (a scaling factor), the radius distribution parameters $f(R_1) \mu$, $f(R_1) \sigma$, $g(R_2) \mu$ and $g(R_2) \sigma$, a background parameter and a sample misalignment parameter ψ_{offset} . This fit results in size distributions with parameters as shown in Table 2 ('Original model'), indicating the presence of a large variance of the distributions of sizes, in accordance with the conclusions of Wang *et al.* (1993). The residuals are small but show systematic deviations. This indicates that the model, whilst good, leaves

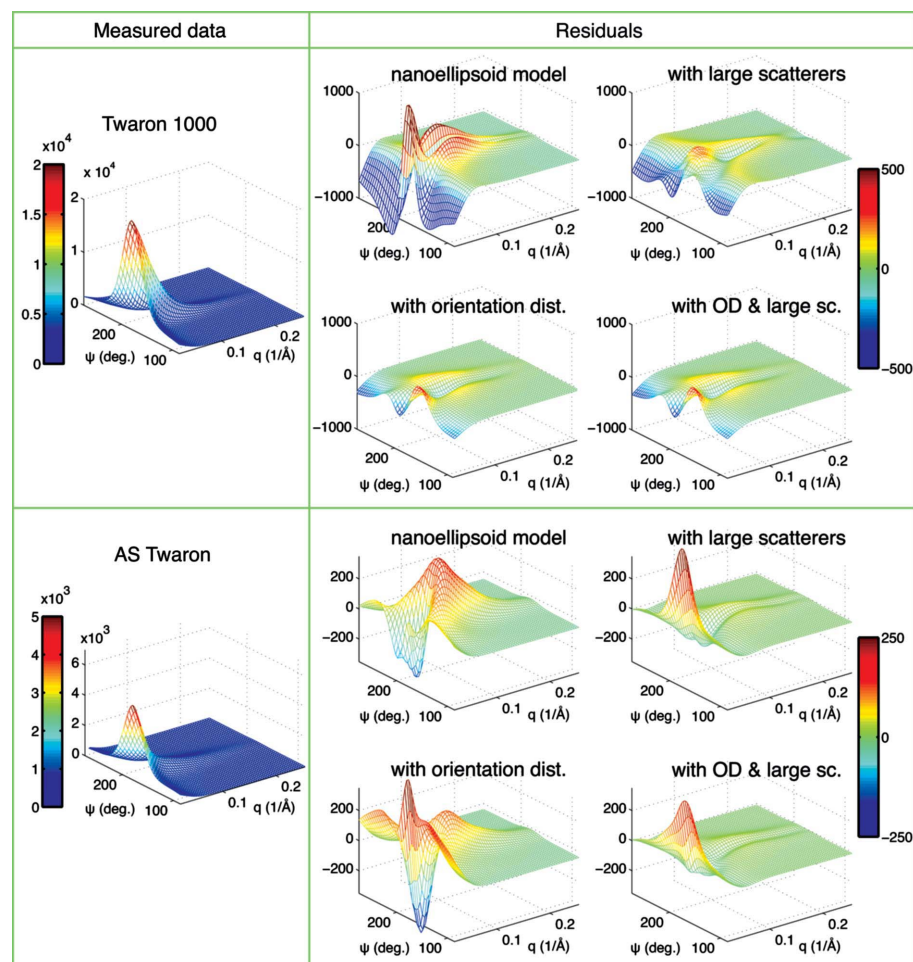

Figure 10

Table of residuals for two modifications of the fit. For Twaron 1000, the best adaptation is the inclusion of an orientation distribution, whereas for as-spun Twaron, additional (large) scatterers improve the fit considerably. Residuals are shown on a vertical scale 20 times that of the data.

Table 2

Fitting results (size parameters are given in Å).

Original model.

Sample	$f(R_1)$ μ (mode)	$f(R_1)$ σ	$g(R_2)$ μ (mode)	$g(R_2)$ σ	ε^2
Twaron 1000	18.3 (15.1)	47.0	101 (45.9)	7060	189
AS Twaron	22.9 (12.8)	249	117 (16.0)	3.79×10^4	132

Model with additional large scatterers.

Sample	$f(R_1)$ μ (mode)	$f(R_1)$ σ	$g(R_2)$ μ (mode)	$g(R_2)$ σ	R_{L1}	α	ε^2
Twaron 1000	4.31 (0.66)	46.6	77.4 (52.7)	1750	36	8.22	118
AS Twaron	12.4 (9.00)	36.6	57.7 (26.2)	2310	121	9.75	60

Model with orientation distribution.

Sample	$f(R_1)$ μ (mode)	$f(R_1)$ σ	$g(R_2)$ μ (mode)	$g(R_2)$ σ	κ	ε^2
Twaron 1000	15.0 (11.6)	42.1	93.5 (17.3)	1.82×10^4	103	87.6
AS Twaron	18.8 (11.8)	130	97.7 (4.91)	6.05×10^4	154	130

Model with orientation distribution and additional large scatterers.

Sample	$f(R_1)$ μ (mode)	$f(R_1)$ σ	$g(R_2)$ μ (mode)	$g(R_2)$ σ	κ	R_{L1}	ε^2
Twaron 1000	15.2 (11.9)	41.0	93.4 (19.0)	1.69×10^4	108	137	87.5
AS Twaron	11.9 (8.97)	29.4	55.0 (28.6)	1.69×10^3	1060	131	58.0

some intensity unaccounted for. This intensity may be partly due to the shape, orientation and size distribution assumptions, which will be addressed shortly.

For the precursor material, *i.e.* the as-spun (AS) Twaron, the fit of the new data analysis model is not satisfactory. Much residual intensity remains, particularly at higher q (see Fig. 10). As indicated above, when the classical models were discussed, the scattering at low q in the AS Twaron scattering pattern shows a contribution from large scatterers. Thus, our new data analysis model fails here, since only a log-normal distribution is considered and not a bimodal distribution.

Given the residuals for both Twaron 1000 and AS Twaron, it has become necessary to address the causes of the discrepancy. Two adaptations of the model are discussed here, which are the addition of a large scatterer to take the low- q scattering into account, and the addition of an orientation distribution to test the assumption of perfectly aligned ellipsoids. Finally, the inclusion of both adaptations in a single model is discussed.

The numerical results from the fitting procedure for various models are given in Table 2. The squared sum of residuals (in arbitrary units) is also given to facilitate comparisons. The residuals are graphically displayed in Fig. 10, so that systematic deviations from the model can be shown.

The accuracy of the resulting parameters can be estimated through calculation of the coefficients of variance. These have been determined from measurements recorded on the DTU Risø rotating-anode-based SAXS instrument. The coefficients of variance are given in % in Table 3 and are shown to be small even for a laboratory source; a good characterization of the

Table 3

Coefficients of variance for the model parameters in %.

Original model.

Sample	$f(R_1)$ CV_μ	$f(R_1)$ CV_σ	$g(R_2)$ CV_μ	$g(R_2)$ CV_σ
Twaron 1000	2.7	2.8	1.4	4.5
AS Twaron	2.6	7.8	2.9	12.2

Model with orientation distribution.

Sample	$f(R_1)$ CV_μ	$f(R_1)$ CV_σ	$g(R_2)$ CV_μ	$g(R_2)$ CV_σ	CV_κ
Twaron 1000	3.7	2.4	1.3	5.5	7.1

Model with additional large scatterers.

Sample	$f(R_1)$ CV_μ	$f(R_1)$ CV_σ	$g(R_2)$ CV_μ	$g(R_2)$ CV_σ	CV R_{L1}	CV_α
AS Twaron	1.9	11.5	2.0	5.9	0.37	7.6

Model with orientation distribution and additional large scatterers.

Sample	$f(R_1)$ CV_μ	$f(R_1)$ CV_σ	$g(R_2)$ CV_μ	$g(R_2)$ CV_σ	CV R_{L1}	CV_κ
Twaron 1000	43	22	50	1.6	5.8	7.9
AS Twaron	1.8	9.3	1.1	1.5	1.8	24

material can therefore also be obtained from measurements obtained from a laboratory source. One exception is the coefficient of variance of the width of the radius distribution of the model modified with an additional large scatterer, which is 11.5%. This is likely due to the additional scattering from the large object.

The results in Table 2 and Fig. 10 show that for Twaron 1000 the residuals are reduced slightly when an additional scatterer is introduced, but systematic deviations remain. Considering a simple (single-parameter) orientation distribution, however, reduces most of the remaining residuals from the original plot, and has a more drastic effect on the squared sum of residuals. The orientation distribution width has an FWHM of approximately 13.4° around its mean. These results clearly indicate that the fit to the data can be improved by considering an orientation distribution, and the resulting modelled intensity now more closely follows the scattering pattern as shown in Fig. 11.

The results for AS Twaron, however, tell a different story. There, the inclusion of an orientation distribution results in a narrow width of the orientation distribution (high value of κ), slightly reducing the sum of squared residuals. A much greater improvement, however, is achieved when large-sized scatterers are introduced in the model. This deviation from the log-normal distribution indicates that there is a bimodal distribution present in these fibres, as previously indicated with the bimodal Debye–Bueche model. The sizes that are now obtained (*cf.* Table 2) for the nanopore distributions are significantly different from those obtained using the unmodified model. This shows that substantial errors in size estimates

can be made if only a single model is used for analysis of both types of fibres, leading to equally erroneous conclusions.

Other results, published elsewhere, show a high degree of orientation of large scatterers present in these fibres (Pauw *et al.*, 2010), much more perfectly aligned than the orientation distribution found for the small scatterers here. This supports the hypothesis that there are separate distributions of scatterers present, one representing (well oriented) fibrillar scattering, and one originating from a void structure which has been characterized here. Results by Grubb *et al.* (1991) also support the notion of a bimodal distribution. They suggested that differently sized scatterers may be present in the core and shell of the PPTA material. Using on-axis microbeam diffraction Davies *et al.* (2008) also noted a difference in the small-angle scattering patterns originating from the shell of the material as compared to the core, concluding that differently shaped scatterers are present in the shell and the core of the material.

Finally, a model can be construed containing both adaptations, the results of which may be better suited for comparison of the nanostructural differences between the two different fibre types. In this model, in order to keep the number of fitting parameters to a minimum, the sample misalignment parameter ψ_{offset} and the large scatterer aspect ratio assume

values obtained from the previous model fits and are fixed. With this, the total number of fitting parameters is limited to nine. The results of the application of this model show that the residuals approach those of the models with a single adaptation, and the resulting parameters equally agree. The drastically increased coefficients of variance (CV) for Twaron 1000, however, indicate that the combination of the adaptations in a single model may result in a more unstable model, and is therefore less suited (especially for measurements obtained using laboratory sources). Application of the combined model to AS Twaron shows that the orientation distribution is very narrow. The models with separate adaptations should therefore be the preferred method of fitting to keep the number of fitted parameters to a minimum, to ensure a stable model that produces reliable results.

From the results for as-spun and heat-treated Twaron (Twaron 1000), some conclusions may be drawn on the changes in internal structure upon heat treatment. To draw these conclusions, the parameters obtained for Twaron 1000 using the model with the orientation distribution are compared with the parameters obtained for AS Twaron using the model with the additional large scatterers. While the results for the fibres from the combined model agree with the results from the previous two, the large coefficient of variance

implies that these values are less reliable for the model combining large scatterers as well as an orientation distribution. The changes in the pore structure after heat treatment are significant, as can be concluded from Fig. 12 and Table 2. On the left-hand side of Fig. 12 the size distributions are visualized as the ellipsoids they represent. The mode has been plotted as the thick solid line, the mean as the dashed line and the 90% confidence interval as the shaded area. From this figure, it is clear that the short-axis radius distribution of the ellipsoids is rather narrow, whereas there is a large variance in the long-axis radius of the scatterers.

The mean lateral pore radius increases through heat treatment from 12.4 to 15.0 Å. The change in the mode of the distribution from 9.00 to 11.6 Å is in good agreement with the change in correlation lengths obtained from the Debye–Bueche method of 8.35 to 12.9 Å. The mode of the longitudinal size distribution of the scatterers (Fig. 12) shifts downward from 26.2 to 17.3 Å, but the mean longitudinal scatterer radius increases from 57.7 to 93.5 Å as a result of the significantly larger tail of the distribution. The σ parameter of especially the longitudinal distribution increases significantly after

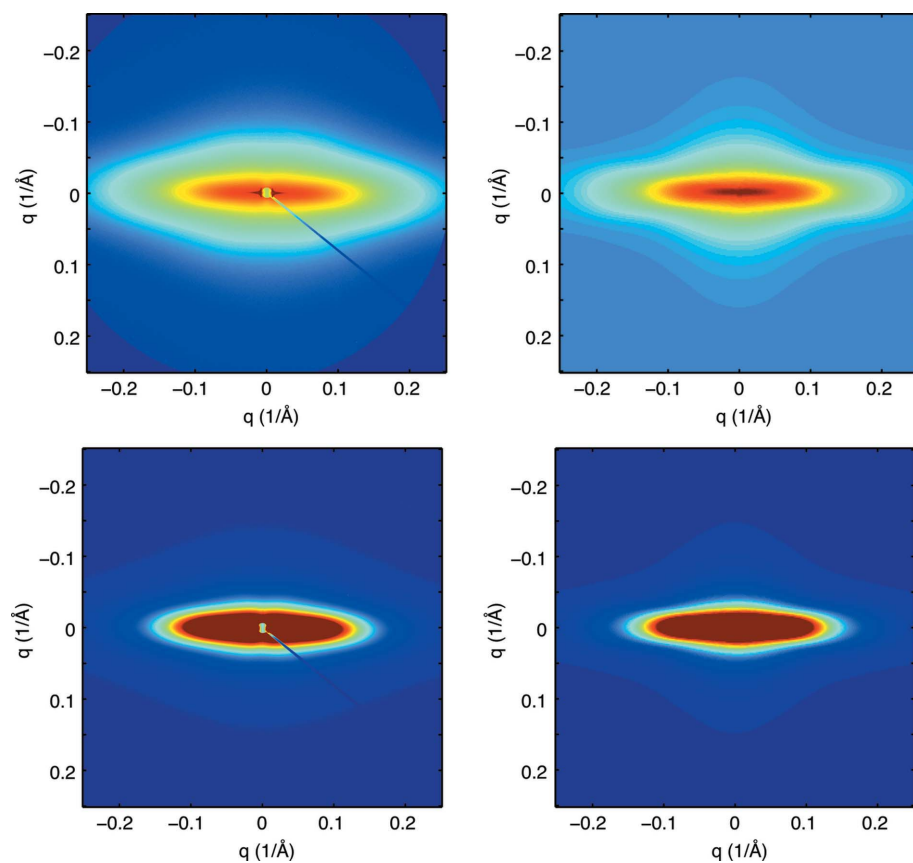


Figure 11

Side-by-side comparison of the scattering pattern (left-hand side) obtained from a bundle of Twaron 1000 filaments mounted vertically and the scattering pattern from the fitting model modified with an orientation distribution (right-hand side). Intensity shown on a logarithmic scale (top) and on a linear scale (bottom).

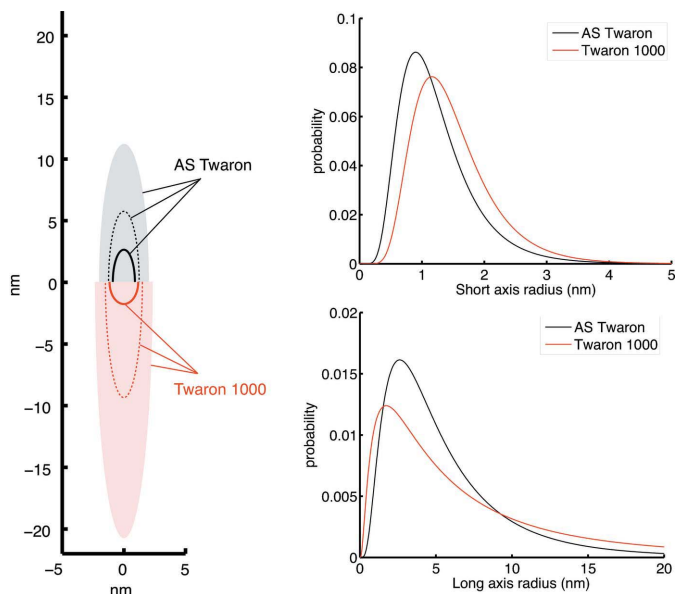


Figure 12

The radius distributions of AS Twaron and Twaron 1000 shown as ellipsoids (left) indicating the maximum likelihood estimator (solid line), mean (dashed line) and 90% confidence interval (shaded areas) of the probability curves shown on the right.

heat treatment. The additional large scatterer contribution required to model the scattering intensity from AS Twaron is no longer required for Twaron 1000, indicating that the heat treatment makes the contribution from the large scatterers less prominent.

These findings are in agreement with measurements obtained using a slit-collimated Kratky camera (Klop, 2001), where it was concluded that the heat treatment causes the small voids to be sintered, shifting the average size of the pores upward. This sintering closes the gaps between the fibrils, effecting the shift of the fibrillar scattering to q angles beyond the resolution of the SAXS instrument (*i.e.* the scattered intensity disappears below the beamstop). This then reduces the contribution of the large scatterers to the scattering pattern. The overall length of the scatterers increases, just like the σ parameter of the distribution. The sintering may well be linked to increases in crystallite sizes upon heat treatment (Jackson *et al.*, 1994). Lastly, the increase in significance of the orientation distribution of the void structure in Twaron 1000 is likely to be related to the increase in prominence of the small void contribution rather than to a real increase in void disorientation, as an *increase* of crystallite orientation has been observed with more stringent heat treatments (Krause *et al.*, 1989; Rao *et al.*, 2001a).

5. Conclusions

The classical analysis methods (the Effler invariant method and the Ruland streak method) for the determination of the orientation distribution of scatterers in aramid fibres are insufficient for the determination of the degree of orientation

for these scatterers. The application of the analysis models to simulated data and real data supports the notion that the main issue is the relatively low aspect ratio of the scatterers. The low aspect ratio causes off-axis contributions to the intensity that are interpreted as originating from the orientation distribution, whilst they are solely due to the scattering by the (near) perfectly aligned scatterer. The determination of the degree of alignment through the Effler invariant method is shown to be highly affected when the aspect ratio of the particles approaches unity, and thus this method can only provide information on either aspect ratio or the degree of alignment.

The analysis of the characteristic length scales of the scatterers present shows that the application of the Debye–Bueche analysis model works. The resulting correlation length (approximating the void size) can be identified as the mode of the radius distribution of the scatterers in that particular direction. For samples with two distinctly different-sized scatterers, a ‘double Debye’ bimodal function can be construed.

Application of the nano-ellipsoid model presented in this paper shows that the assumptions made are reasonable for describing most of the intensity found in the scattering patterns. The nano-ellipsoid model is based on a system of ellipsoidal scatterers that are perfectly oriented with respect to the fibre axis. It is assumed that the size distributions of these scatterers can be described by log-normal distributions. Furthermore, the scatterers are assumed to be non-interacting, implying that they are allowed to intersect.

Adaptations of the model improve the obtained fits and may significantly affect the size parameters obtained. One adaptation required for the modelling of the scattering pattern of the as-spun aramid material is that a large-sized scatterer should be included. A second adaptation that was employed for analysis of the scattering pattern of Twaron 1000 is the introduction of an (in-plane) orientation distribution.

The application of the nano-ellipsoid model to the aramid yarn samples shows that the heat treatment effects an increase in overall void size and distribution widths, both laterally as well as longitudinally, suggesting that the smaller voids are sintered away during the heat treatment. The interfaces between fibrils similarly disappear, making the fibrillar structure much larger. This then causes a shift of the large scattering contribution seen in AS Twaron to below the detection limits of the instrument.

MAX-lab in Lund, Sweden, is acknowledged for SAXS beamtime at the I711 beamline. This work was supported by DanScatt, the Danish Centre for the Use of Synchrotron X-ray and Neutron Facilities, sponsored by the Danish Research Council for Nature and the Universe, and by Teijin Aramid BV. The authors would also like to acknowledge P. Malchev at Teijin Aramid for his work on the implementation of the orientation distribution, and K. D. Joensen of JJ X-ray Systems A/S for his assistance with the *SAXSGUI* package.

References

- Aerts, J. (1991). *J. Appl. Cryst.* **24**, 709–711.
- Chae, H. G. & Kumar, S. (2006). *J. Appl. Polym. Sci.* **100**, 791–802.
- Ciccariello, S. (1993). *Acta Cryst.* **A49**, 750–755.
- Ciccariello, S., Schneider, J.-M., Schönfeld, B. & Kistorz, G. (2002). *J. Appl. Cryst.* **35**, 304–313.
- Crow, E. L. & Shimizu, K. (1988). *Lognormal Distributions: Theory and Applications*, 1st ed. New York: Marcel Dekker Inc.
- Davies, R. J., Koenig, C., Burghammer, M. & Riekel, C. (2008). *Appl. Phys. Lett.* **92**, 101903.
- Debye, P., Anderson, H. R. Jr & Brumberger, H. (1957). *J. Appl. Phys.* **28**, 679–683.
- Debye, P. & Bueche, A. M. (1949). *J. Appl. Phys.* **20**, 518–525.
- Diez, B. & Sobry, R. (1993). *J. Phys. IV*, **3**, 511–513.
- Dobb, M. G., Johnson, D. J., Majeed, A. & Saville, B. P. (1979). *Polymer*, **20**, 1284–1288.
- Dobb, M. G., Johnson, D. J. & Saville, B. P. (1977). *J. Polym. Sci. Polym. Symp.* **58**, 237–251.
- Effler, L. J. & Fellers, J. F. (1992). *J. Phys. D Appl. Phys.* **25**, 74–78.
- Evans, M., Hastings, N. A. J. & Peacock, J. B. (2000). *Statistical Distributions*, Wiley Series in Probability and Statistics, Vol. 359. New York: Wiley Interscience.
- Glatter, O. & Kratky, O. (1982). *Small-Angle X-ray Scattering*. London: Academic Press.
- Grubb, D. T., Prasad, K. & Adams, W. W. (1991). *Polymer*, **32**, 1167–1172.
- Guinier, A. & Fournet, G. (1955). *Small-Angle Scattering of X-rays*. New York: Wiley.
- Helfer, E., Panine, P., Carlier, M.-F. & Davidson, P. (2005). *Biophys. J.* **89**, 543–553.
- Hermans, P. H., Heikens, D. & Weidinger, A. (1959). *J. Polym. Sci.* **35**, 145–165.
- Horio, M., Kaneda, T., Ishikawa, S. & Shimamura, K. (1984). *Sen'i Gakkaishi*, **40**, 285–290.
- Jackson, C. L., Schadt, R. J., Gardner, K. H., Chase, D. B., Allen, S. R., Gabara, V. & English, A. D. (1994). *Polymer*, **35**, 1123–1131.
- Jiang, H., Adams, W. W. & Eby, R. K. (1993). *High Performance Polymer Fibres: Material Science and Technology (a Comprehensive Treatment)*, edited by R. W. Cahn, P. Haasen & E. J. Kramer, Vol. 12, ch. 13. New York: VCH.
- Kenig, S. (1987). *Polym. Eng. Sci.* **27**, 887–892.
- Klop, E. A. (2001). *The Investigation of the Microstructure of Aramid Fibres Using Small-Angle X-ray Scattering*. Internal Report, Teijin Aramid BV, Arnhem, The Netherlands.
- Koberstein, J. T., Morra, B. & Stein, R. S. (1980). *J. Appl. Cryst.* **13**, 34–45.
- Krause, S. J., Vezie, D. L. & Adams, W. W. (1989). *Polym. Commun.* **30**, 10–13.
- Mooney, D. A. & MacElroy, J. M. D. (2004). *Chem. Eng. Sci.* **59**, 2159–2170.
- Morgan, R. J., Pruneda, C. O. & Steele, W. J. (1983). *J. Polym. Sci. Polym. Phys. Ed.* **21**, 1757–1783.
- Northolt, M. G. & Aartsen, J. J. van (1973). *J. Polym. Sci. Polym. Lett. Ed.* **11**, 333–337.
- Northolt, M. G. & Sikkema, D. J. (1991). *Adv. Polym. Sci.* **98**, 119–172.
- Northolt, M. G. & Stuut, H. A. (1978). *J. Polym. Sci. Polym. Phys.* **16**, 939–943.
- Panar, M., Avakian, P., Blume, R. C., Gardner, K. H., Gierke, T. D. & Yang, H. H. (1983). *J. Polym. Sci. Polym. Phys. Ed.* **21**, 1955–1969.
- Pauw, B. R., Vigild, M. E., Mortensen, K., Andreasen, J. W., Klop, E. A., Breiby, D. W. & Bunk, O. (2010). *Polymer*. Submitted.
- Pedersen, J. S. (1997). *Adv. Colloid Interface Sci.* **70**, 171–210.
- Perret, R. & Ruland, W. (1969). *J. Appl. Cryst.* **2**, 209–218.
- Perret, R. & Ruland, W. (1970). *J. Appl. Cryst.* **3**, 525–532.
- Picken, S. J., Zwaag, S. van der & Northolt, M. G. (1992). *Polymer*, **33**, 2998–3006.
- Ran, S., Fang, D., Zong, X., Hsiao, B. S., Chu, B. & Cunniff, P. M. (2001). *Polymer*, **42**, 1601–1612.
- Rao, Y., Waddon, A. J. & Farris, R. J. (2001a). *Polymer*, **42**, 5937–5946.
- Rao, Y., Waddon, A. J. & Farris, R. J. (2001b). *Polymer*, **42**, 5925–5935.
- Riekel, C., Cedola, A., Heidelbach, F. & Wegner, K. (1997). *Macromolecules*, **30**, 1033–1037.
- Ruland, W. (1971). *J. Appl. Cryst.* **4**, 70–73.
- Ruland, W. (1978). *Colloid Polym. Sci.* **256**, 932–936.
- Ruland, W. (1990). *Adv. Mater.* **2**, 528–536.
- Saijo, K., Arimoto, O., Hashimoto, T., Fukuda, M. & Kawai, H. (1994). *Polymer*, **35**, 496–503.
- Sawyer, L. C., Chen, R. T., Jamieson, M. G., Musselman, I. H. & Russell, P. E. (1993). *J. Mater. Sci.* **28**, 225–238.
- Schmidt-Rohr, K. (2007). *J. Appl. Cryst.* **40**, 16–25.
- Stribeck, N. (2001). *J. Appl. Cryst.* **34**, 496–503.
- Stribeck, N. (2007). *X-ray Scattering of Soft Matter*. Berlin, Heidelberg: Springer-Verlag.
- Tang, M.-Y., Rice, G., Fellers, J. & Lin, J. (1986). *J. Appl. Phys.* **60**, 803–810.
- Tanner, D., Fitzgerald, J. A. & Phillips, B. R. (1989). *Angew. Chem. Int. Ed. Engl.* **28**, 649–654.
- Wang, W., Ruland, W. & Cohen, Y. (1993). *Acta Polym.* **44**, 273–278.
- Weisstein, E. W. (2005). *Log Normal Distribution*. From *Mathworld*, <http://mathworld.wolfram.com/LogNormalDistribution.html>.
- Weisstein, E. W. (2009). *von Mises Distribution*. From *MathWorld*, <http://mathworld.wolfram.com/vonMisesDistribution.html>.
- Weyland, H. G. (1980). *Polym. Bull.* **3**, 331–337.
- Yabuki, K., Ito, H. & Oota, T. (1976). *Sen'i Gakkaishi*, **32**, T55–T61.